IEEE Access
Multidisciplinary | Rapid Review | Open Access Journal

Received October 2, 2019, accepted October 22, 2019, date of publication October 25, 2019, date of current version November 13, 2019.

Digital Object Identifier 10.1109/ACCESS.2019.2949739

2D Ray Tracing Analysis of a Dynamic Metasurface Antenna as a Smart Motion Detector

OREN S. MIZRAHI, (Student Member, IEEE), MOHAMMADREZA F. IMANI, (Member, IEEE), K. PARKER TROFATTER, JONAH N. GOLLUB, AND DAVID R. SMITH, (Senior Member, IEEE)

Center for Metamaterials and Integrated Plasmonics, Department of Electrical and Computer Engineering, Duke University, Durham, NC 27708, USA

Corresponding author: Oren S. Mizrahi (orensimonmizrahi@gmail.com)

This work was supported in part by the Advanced Research Projects Agency-Energy (ARPA-E), U.S. Department of Energy, under Award DE-AR0000937.

ABSTRACT We present a ray-tracing analysis of a smart motion detector based on a dynamically reconfigurable metasurface antenna (DMA). A DMA consists of an array of metamaterial radiators excited by a single-port waveguide or cavity. By incorporating simple switchable components into each element and addressing them individually, DMAs can generate a myriad of spatially distinct radiation patterns and alter them as a function of an applied voltage. These patterns have the potential to probe all regions of a room or set of rooms and detect motion, even when operating over an extremely narrow bandwidth. Through the acquisition of time-resolved measurements, the DMA sensor can retrieve temporal signatures and distinguish between different sources of movements. We investigate this sensing paradigm using a ray tracing simulation. We first replicate the trends obtained from recent experiments using our simulation platform to ensure that numerical ray tracing generates data that is a faithful representation of the real-life physics. We then demonstrate that temporal signals obtained in this manner carry information about the nature of the movement. Specifically, by using power spectra and filtering, we are able to extract features that correspond to specific motion patterns. These results constitute the first step toward incorporating DMAs into a smart sensor equipped with learning algorithms that can distinguish between human and non-human motion with high fidelity.

INDEX TERMS Ray tracing, antenna radiation patterns, cavity resonators, radio frequency (RF), sensors, antenna arrays.

I. INTRODUCTION

Occupation sensing technology is an indispensable component in the drive towards *smart* buildings and the internet of things (IoT) [1]–[3]. Smart occupancy sensors can adjust heating and cooling settings and are crucial in reducing the energy consumption of residential and commercial buildings [4], [5]. One recent study estimated that such devices could save upwards of 30% in power and cost in the United States [6]. In addition, the utility of an occupancy sensor can be extended to monitor the vital signs of occupants [7]. For example, a non-invasive smart sensor can monitor for distressed breathing rates in individuals with medical conditions like sleep apnea and diabetes [8]. Additional medical applications include monitoring the elderly [9] for falls [10], which stand as a major source of concern and risk in their everyday lives [11].

Despite the growing interest, current occupancy sensors—such as the ubiquitous pyroelectric infrared motion sensors [12]—do not meet the needs of this growing field [13]. Many recent works on smart sensing use radio frequency (RF) and microwave devices as smart occupancy sensors. The appeal of RF and microwave sensors stems from multiple factors. First, RF and microwave devices can easily keep user data anonymous and they are not intrusive into individuals' daily lives. In addition, microwaves can penetrate clothes and furniture and bounce off walls and ceilings, generally increasing the range within which a sensor can operate. This allows RF sensors to operate both in line-of-sight (LOS) and non-line-of-sight (NLOS) scenarios. Moreover, low power microwaves and RF waves are deemed harmless to humans and

The associate editor coordinating the review of this manuscript and approving it for publication was Weiren Zhu.

animals, mitigating health concerns. Given these advantages, there has been a significant push to leverage microwave and RF signals for human presence detection and motion monitoring [14]–[23].

In active microwave sensing without user cooperation (i.e. wearing a tag or carrying an RF device), fluctuations of the received signal are examined to infer human presence. In this framework, the sensor relies on the fact that a human's presence and the inevitable movements (i.e. walking, breathing, etc.) induce tangible fluctuations in the received signal (e.g. micro-Doppler shifts, shadowing on the channel state information, or the received signal strength). This idea has its roots in the physical concept of *diffusing wave spectroscopy* where the fluctuation of waves inside a cavity is monitored to detect and characterize a dynamic scatterer [24]–[28]. Applying this interpretation, a residential building is approximated as an irregular cavity, where microwaves bounce around several times before reaching a receiver. As a result of the cavity's irregular geometry, the wave inside the room resembles a speckle pattern; any perturbation to this speckle pattern can cause significant variations at the receiver. A dynamic (moving) scatterer, such as a human, can cause significant variations in the field at the receiver. Since most rooms are not perfectly reflective and the microwaves attenuate as they propagate, such schemes can be sensitive to noise and it is common to use frequency diversity to increase the reliability of measurements [29]. Alternatively, one can use spatial diversity implemented by an antenna array or sensor network to tap into different modes reverberating inside the room to detect motion with high fidelity.

Recently, the notion of using spatial diversity to detect motion has been demonstrated using a novel hardware: a dynamic metasurface antenna (DMA) [30]. Generally speaking, a DMA—a schematic for which is shown in Figure 1(a)—consists of a waveguide or a cavity exciting an array of metamaterial radiators [31]–[34]. By introducing a switchable component into each element (e.g. a diode) and addressing it individually, the DMA allows for the generation of spatially distinct radiation patterns and their rapid variation without using complex and power hungry components (e.g. phase shifters, switches, etc.). The spatially varying radiation patterns generated by the DMA multiplex the information that could be gathered by a large number of virtual dipole antennas [35], [36]. In this manner, the DMA allows for rapid acquisition of information from an electrically large aperture (or a large antenna array). The spatial diversity realized by a DMA was shown in [30] to drastically improve the sensor's ability to detect motion, even in occluded areas. The applicability of a DMA-based motion detector is further advanced by its relatively low cost. With a PCB construction using only simple electronic components (diodes, varactors, etc.) DMAs are economical to mass-produce, making them an appealing alternative hardware choice for motion detection and occupancy sensing. Using DMAs for detecting motion inside a residential setting is conceptually depicted in Figure 1(b) where the spatial diversity realized by reconfigurable patterns of the DMA are used.

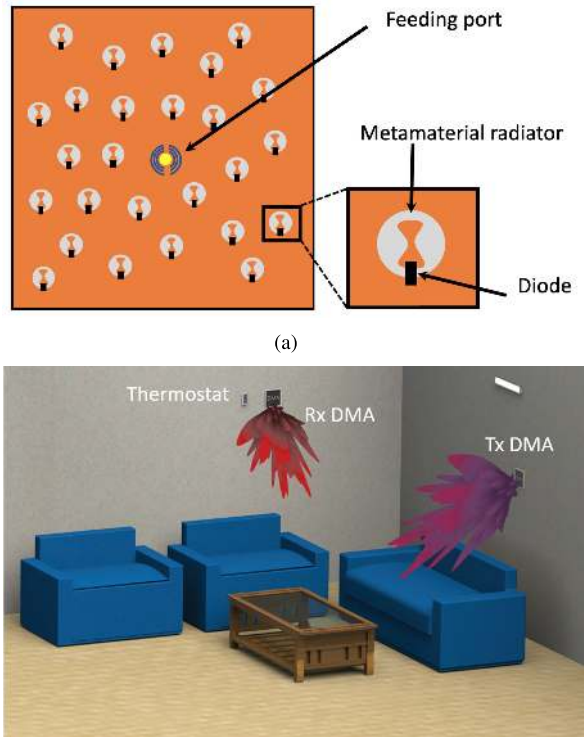

FIGURE 1. **(a) A schematic of the front of a 2D DMA. (b) A residential environment probed for motion with two DMAs.**

Another interesting advantage of using DMAs for sensing application is the elimination of the need for bandwidth. Since DMAs-based sensors can operate at a single frequency [30], they do not pose any interference concern. Single frequency (or narrow bandwidth) operation also significantly simplifies the required RF circuitry and reduces cost. Without concern about interference and circuit complexity, one can also utilize a higher frequency (e.g. 20 GHz, as compared to typical WiFi frequencies) to improve sensitivity and reduce sensor size.

Single frequency operation, however, prevents us from utilizing micro-Doppler signatures, which are commonly used to determine the source and type of motion. While this limitation may seem to hinder DMAs' functionality as *smart* devices, we note that DMAs can acquire temporal signature of movements. This capability is due to the DMA's simple circuitry which allows for rapid switching between its radiation patterns; A DMA-based sensor is thus able to obtain information at speeds far in excess of typical motion. Hence, a DMA-based sensor should be able to generate a temporal signal with the necessary sampling frequency to identify and distinguish different motion patterns.

In this work, we present a ray-tracing simulation platform that enables us to further test and investigate DMA-based sensors. Ray-tracing allows us to approximate the behavior of the DMA as a motion sensor. While not a replacement for physical experiment, simulations allow us to generate

large quantities of data for different motion patterns, room geometries, DMA configurations, etc. We can control motion patterns and physical variables in a quick and repeatable way that would be unfeasible in experiment. Ray-tracing also enables us to develop an intuition for the signals generated under these varied circumstances. Building on the work in [30]—which was done in a small metallic cavity—we use the ray-tracing simulation system to demonstrate the advantage of using a DMA for motion sensing in a residential environment. We further demonstrate that signals obtained from these simulations reflect the characteristics of motion patterns that caused them, giving us confidence that such a system can be paired with learning algorithms to classify and detect motion in real-time.

This paper is organized as follows: After describing our ray tracer, we demonstrate that our system provides a faithful representation of a DMA operating in a disordered cavity (i.e. residential room). Next, we use ray-tracing simulations to highlight the DMA's advantages as a motion detector by demonstrating extremely low false negative detection rates. Lastly, we demonstrate that the temporal signal retrieved by a DMA exhibits features corresponding to movements in the room, demonstrating DMA's potential viability as a *smart* motion sensor.

II. RAY TRACING INSIDE A ROOM

Ray tracing has been extensively used to model the propagation of waves inside an indoor environment [37]–[44]. Depending on the desired accuracy and computational power, a variety of physical phenomena can be incorporated, such as reflection, refraction, diffraction, and diffusion [44]–[46]. Ray tracing has proven to be a useful technique to obtain physical insight into the evolution of an electromagnetic wave as it traverses a closed environment, and can be used to evaluate the performance of certain systems, e.g. a communication link [37]–[44]. Ray tracing also requires a lower computational cost than other simulation techniques—e.g. full-wave simulations, which are prohibitively time consuming. Our goal here is to use ray tracing as a simple and fast tool to demonstrate the utility of DMAs in detecting and characterizing dynamic scatterers inside a room; we do not intend to develop a platform that can replace real life measurements.

The ray tracing model used throughout this manuscript is detailed in the Appendix A. It is worth noting that for simplicity and speed, we develop our tracing algorithm in two dimensions (2D). This can be interpreted as modeling the cross section of the room depicted in Figure 1. To further simplify the simulation process, we use omnidirectional point antennas to model each transmitter (Tx) and receiver (Rx). Such an assumption closely resembles many practical scenarios, for example when using dipole or monopole antennas with their axes aligned perpendicular to the plane of simulation.

With the exception of Section 5 and the latter two plots in the Appendix A, the generic room—referred to as *Room 1* and shown in Figure 2—will be used as the geometry for simulations. As an example, the evolution of the signal

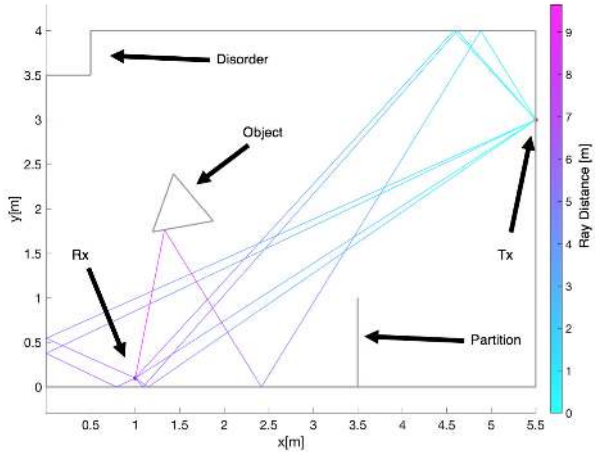

FIGURE 2. A snapshot of one frame of ray tracing simulation in *Room 1*. Rays are capped at 3 reflections.

from a single antenna Tx to a single Rx antenna, calculated using our ray tracing model, is also depicted. A small partition and corner are added to further resemble a typical room. The Tx antenna is placed at (5.5 m, 3 m), while the Rx antenna is placed at a (1m, 0.1 m). The room size is 5.5 m by 4 m, which is typical for many real-life scenarios. For simplicity and faster simulation speeds, we model objects/humans as equilateral triangles, as shown in Figure 2. The triangle size and orientation is adjusted according to the specific scenario: human breathing is modeled as a sinusoidal variation of the triangle side length between 40 cm and 41 cm (at a frequency of 0.2 Hz, typical of a human adult [47]), while fan movement is modeled as rotation around the centroid of a triangle (triangle side is 40 cm, rotation is at a frequency of $\approx$ 57 Hz). In all the studies throughout this paper, we assume a stop-motion process: the object is assumed to be stationary during each instantaneous measurement.

Because the ray-tracing algorithm is recursive, we are required to establish a *cap* on the number of times rays can bounce off of objects and walls before reaching the receiver. Because of losses incurred as a result of reflection and propagation over large distances, there is diminishing return to setting a larger cap which will be more physically accurate but will incur exponentially large run-times. After investigating this trade-off numerically (see Appendix A), we decided to set the cap at 3 bounces for *Room 1*.

A. DYNAMIC METASURFACE APERTURE MODEL

We use omnidirectional point antennas to emulate simple Tx and Rx antennas. This model is a reasonable representation of most antennas used in current RF occupancy sensors (e.g. WiFi router antennas). By contrast, instead of an omnidirectional pattern, a DMA generates a complex radiation pattern exhibiting many lobes in all directions [31]–[34]. When the aperture field distribution (referred here as a *mask*) of the DMA changes, the complex pattern also changes.

A typical DMA would consist of an array of metamaterial irises inserted into the upper conductor of either a waveguide or a cavity (see Figure 1b). Each element radiates as

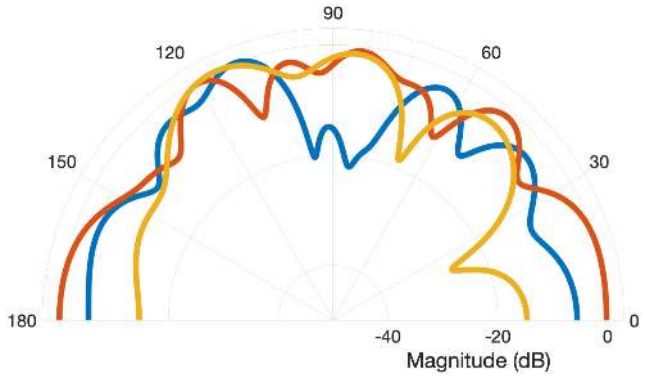

FIGURE 3. Far-field normalized directivity patterns for a modulated 8-dipole array with 3 random *mask* configurations.

a magnetic dipole, such that the radiation pattern for the composite antenna can be expressed as a sum of dipoles, each with an amplitude and phase dictated by the field in the waveguide or cavity at the position of the dipole. Since our goal here is to produce radiation patterns that are generally random, we model the DMA as an array of 8 dipoles, spaced $\lambda/2$ apart and with random phase and random binary amplitude (λ is the wavelength in free space). As an example, we have generated 3 such masks, with binary amplitude and phase shown in Table 1. We have simulated far-field directivity plots for these masks and displayed them in Fig. 3. As shown in Fig. 3, modulating the mask pattern in this way generates diverse radiation patterns. This representation of a DMA produces directivity patterns consistent with those of an actual fabricated DMA characterized using near field scanning techniques [32]–[34], [48].

TABLE 1. Binary amplitude (P) and phase (ϕ, rad) values for 8-dipole "DMA" with 3 random masks.

		1	2	3	4	5	6	7	8
bl.	P	1	1	1	1	1	0	0	1
	ϕ	2.96	0.27	0.61	4.54	3.26	5.03	5.19	1.09
red	P	1	0	1	1	1	0	0	1
	ϕ	0.37	0.45	5.14	0.94	6.11	2.85	0.52	2.46
yel.	P	0	0	0	1	1	1	0	1
	ϕ	4.29	3.28	5.14	4.14	4.08	2.72	0.84	5.22

For each dipole used to represent the DMA, at each simulated time-step, the ray tracing algorithm is conducted separately, resulting in a matrix of $N_t \times N_{\mathrm{Tx}} N_{\mathrm{Rx}}$ signals, where N_t is the number of time samples, N_{Tx} is the number of dipoles in the transmitting array, and N_{Tx} is the number of dipoles in the receiving array. The complex amplitude of the signal emanating from the Tx dipole i and propagating to the Rx dipole k at time t is given by summing over the complex amplitudes of all rays between these two points: $S_{i,k}(t) = \sum_r S_{i,k}(r,t)$, where $S_{i,k}(r,t)$ is the complex amplitude of a given ray. $S_{i,k}(r,t)$ is given in Equation 9 and is discussed in the Appendix. The received signal, W, is then computed accordingly:

$$W(t, m_{\mathrm{Tx}}, m_{\mathrm{Rx}}) = \sum_{i=1}^{N_{\mathrm{Tx}}} \sum_{k=1}^{N_{\mathrm{Rx}}} \mathrm{mask}(m_{\mathrm{Tx}}, i)\mathrm{mask}(m_{\mathrm{Rx}}, k) S_{i,k}(t) \tag{1}$$

where

$$\mathrm{mask}(m, i) = \frac{P_{m,i} e^{j\phi_{m,i}}}{\sqrt{\sum_i P_{m,i}}} \tag{2}$$

is a phase and amplitude modulating function with randomly generated phase ($\phi_{m,i} \in [0, 2\pi)$) and amplitude ($P_{m,i} \in \{0, 1\}$). The values of $\phi_{m,i}$ and $P_{m,i}$ can change for each mask and dipole. The denominator in (2) normalizes mask's amplitudes so that all masks have comparable power which is equal to that of a single dipole. Thus, because $P_{m,i}$ is either 0 or 1 and because the normalizing denominator in Equation 2 is the same for all dipoles active in a mask, all dipoles always output equal power.

It is important to note that a DMA can serve as a transmitter, receiver, or both. In Eq. 1, we consider the case of using a DMA as both the transmitter and receiver. If one of the antennas were a single dipole, we would mathematically model it as a DMA with one dipole and a constant mask function mask(m, i), where $m, i = 1, P_{1,1} = 1$, and $\phi_{1,1} = 0$. This would simplify our signal matrix to $W(t, m)$, where t iterates over time and m iterates over DMA masks.

For a DMA modeled by N_d dipoles there are a multitude of possible masks with which to configure the array of dipoles. By simulating dipole signals individually and calculating masks in post-simulation analysis, we are able to save significant time and computational cost while examining an exponentially large number of masks (and equivalently, large number of complex radiation patterns). More specifically, instead of running N_m ray tracing simulations, we only run N_d ray tracing simulations. Given that in most practical implementations, $N_d \ll N_m$, we are able to simplify our simulations considerably.

III. DATA ANALYSIS METHODOLOGY

A. PROCESSING OF RECEIVER DATA

The signal received by the Rx antenna consists of two components: the static component, which can be attributed to rays that do not interact with the moving object, and the dynamic component, which varies as the object occludes rays' paths or changes their trajectories [24]–[27], [29], [45]. The static component of the signal is usually a function of room geometry and objects in the room; it can often dominate the dynamic component of the signal and doesn't interest us for motion detection purposes. Thus, our goal becomes finding a way to remove the static component of the signal.

One historical approach to this problem is taking an initial measurement in the room while it is known there is no motion. Without motion, this signal is completely due to the room geometry. Thus, this "calibration measurement" can be subtracted from subsequent measurements where motion is taking place to isolate the dynamic component caused by motion. However, if, for example, a chair is moved, or a closet door is opened, our room geometry changes and a new calibration measurement must be taken. It's clear that this is an ineffective method for our purposes.

Instead, we can simply assume that the dynamic component of the signal is changing between measurements whereas the static component almost always remains constant between measurements. Thus, to isolate the dynamic component, we simply need to subtract the previous measurement from each measurement. In doing so, we are effectively ''continuously calibrating'' our system.

Mathematically, this process can be described as follows: assume the signal received by a receiver is given by $W(t, m)$, where $m \in \{1, 2, .., N_m\}$ is the selected mask, $t \in \{1, 2, .., N_s\}$ is the current time sample and N_s is the number of samples. We then define the following difference function:

$$D(t, m) = W(t + 1, m) - W(t, m), \tag{3}$$

which is the temporal fluctuation for different masks.

B. SAMPLING RATE

Our goal is to investigate DMAs as motion detector that can also differentiate between different sources of motion based on their temporal fluctuation signatures. This requires that the Tx and Rx apertures can monitor the scene at a rate high enough to capture temporal variations accurately. However, high frequency sampling burdens the hardware, consumes power, and can potentially require greater memory allocation. To determine a reasonable sampling rate that accurately captures the events within a regular room with minimal burden on hardware, we investigate various motion patterns common to everyday life.

In most residential settings, motorized moving objects such as fans, washing machines, or dryers, etc. are the sources of the highest frequency mechanical motion. Traditionally, the Nyquist frequency (twice the frequency to be detected) gives the sampling frequency that will eliminate aliasing. However, in the simulations considered here, a rotating fan at 60 Hz does not necessarily result in a 60 Hz sinusoidal signal. This phenomenon is illustrated in the following example. We have simulated a fan located at (1 m,2 m) rotating at f_0. Due to the rotational symmetry of the equilateral triangle used, we set the rotational frequency to be $\frac{f_0}{3}$ to emulate a fan rotating at f_0. We use a DMA with a single, fixed mask as a transmitter and a single dipole as a receiver; the same phenomenon can be demonstrated for a single dipole transmitter or for a DMA with many masks. The signal received in this study, given by $D(t)$, is plotted in Figure 4 (a). For this simulation, the triangle had a diameter of 40 cm and a rotation frequency of $f_0 = 60$ Hz. The received signal was sampled at 1 kHz. We clearly see rapid fluctuation of the dynamic signal, even though the sampling frequency is an order of magnitude higher than the motion frequency to be detected.

This phenomenon, which resembles aliasing, can be detrimental to the occupancy sensor proposed here: the signal due to a rotating fan aliases to lower frequencies or appears aperiodic, and can easily confuse a classifying algorithm that is based on detecting features in the temporal signal. The aliasing effect is more evident when examining the autocorrelation and power spectrum of the received signal. To do that, we have computed the autocorrelation of a discrete time series, $f(t)$ using (4), where l is the lag time, N_t is the number of time samples, and $\bar{f}$ is the mean of all values of f:

$$\widetilde{A}(l) = \frac{\frac{1}{N_t}\sum_{i=1}^{N_t}(f(t_i) - \bar{f})(f(t_i + l) - \bar{f})}{\frac{1}{N_t - 1}\sum_{i=1}^{N_t}|f(t_i) - \bar{f}|^2} \tag{4}$$

Similarly, we computed the power spectra given using the discrete fast-Fourier transform (DFFT), defined below at an angular frequency ω, for the same time series, $f(t)$:

$$\widetilde{F}(\omega) = \sum_{i=1}^{N_t} f(t_i) e^{\frac{-j\omega i}{N_t}} \tag{5}$$

The autocorelation and the power spectrum of the received signal computed in this manner are shown in Fig. 4 (c) and 4 (e). We clearly see that although the object under test is a fan rotating at 60 Hz, we see frequency content aliased all over the spectrum.

To understand the reason behind rapid variation of the received signal and its aliasing, we need to examine the physics of the system at hand more closely. The irregularly shaped room considered here, akin to most practical settings, acts as a cavity for the microwaves. The waves bounce around and interfere with each other, forming a speckle-looking pattern inside the room. Once the object moves in this setting, it perturbs the field pattern formed within the room, resulting in fluctuation of the received signal. As documented in diffusing wave spectroscopy literature [24], such detection schemes are extremely sensitive to even small changes (less than half of a wavelength). At our sampling frequency of 1 kHz, rotation of a triangle at 60 Hz results in a displacement of 21° every time a sample is taken. Such a large variation in angular position causes the ray pattern of the scene to vary significantly frame to frame. As a result, the received signal exhibits rapid fluctuations with (temporal) frequency content much larger than the actual target rotation.

In real-life, RF electronic circuitry does not sample a signal instantaneously. Instead, it captures the received signal during a finite duration, commonly referred to as an integration time or an exposure time. Incorporating an integration time into our model allows us to average out the rapid fluctuation due to high sensitivity of received signal to small perturbations. To model integration time in our simulation platform, we instantaneously sample the room N_I times over the desired integration period and coherently average these samples. The signal stored in the received signal from Tx dipole i to Rx dipole k, $S_{i,k}(t)$, is then the result of these complex sums, generated at a sampling rate of f_s.

From a design perspective, we have two ''knobs'' to turn in our simulations: sampling rate, f_s, and the duration of the integration time. Additionally, because we emulate the analog process of taking a measurement over an integration time using discrete samples, the number of samples per integration time (N_I) play a crucial role in ensuring a faithful representation of real-life scenarios. The integration time, while crucial to practical implementations, is heavily dependent on

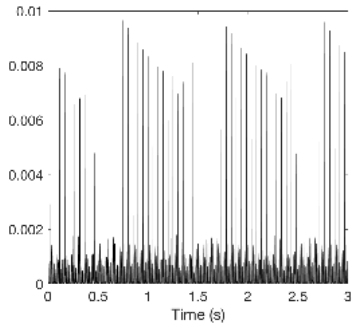

(a) $D(t)$ with instantaneous sampling

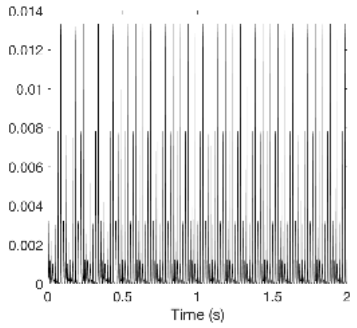

(b) $D(t)$ with integration time

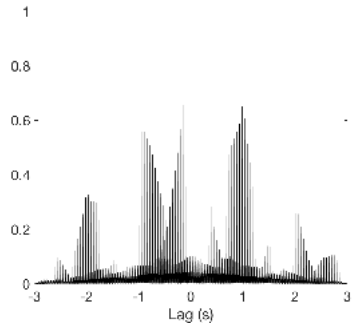

(c) Autocorrelation of $D(t)$ with instantaneous sampling

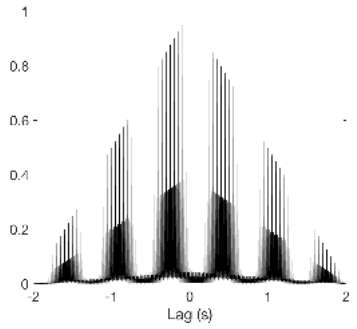

(d) Autocorrelation of $D(t)$ with integration time

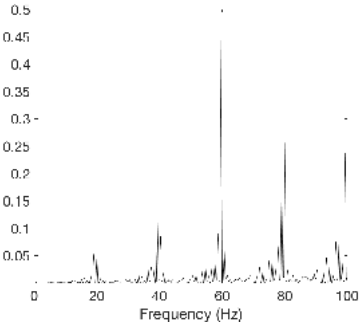

(e) Power spectrum of $D(t)$ with instantaneous sampling

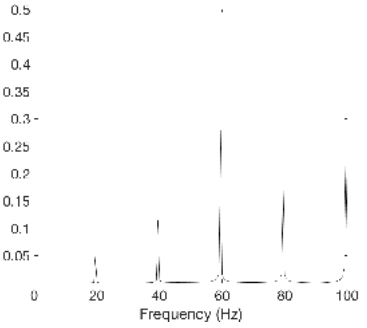

(f) Power spectrum of $D(t)$ with integration time

FIGURE 4. **Demonstrating the benefit of incorporating an integration time into the simulation sampling regime. (a) and (b) were generated in *Room 1*, with wooden walls and a reflection cap of 3. Tx is a 3-dipole array, Rx is a single dipole.**

the choice and cost of hardware and does not fit into our studies. Thus, we assume a constant integration time.

The choice of sampling rate thus requires thorough analyses. Too low a sampling rate will lead to aliasing and will not accurately capture the motion patterns; alternatively, too high a sampling rate and the simulation will incur long runtimes that may be unnecessary. As before, we focus here on striking a balance between simulation accuracy and unnecessary runtimes. More critical, however, is ensuring that the number of sampling points within an integration time is high enough to be a statistically accurate representation of the state of the signal.

With these considerations in mind, we used the following setting in our studies: to emulate an IF bandwidth of about 2 kHz—a value often achievable for most off-the-shelf components—we set the integration time per sample to 470 μs. This value is small enough that a triangle rotating at about 60 Hz will not rotate significantly during integration. We then performed a number of studies to obtain appropriate values for f_s and N_I. Our goal was to obtain a relatively unaliased receive signal when monitoring a fan, while keeping the lowest f_s possible. We tested values of $f_s = 200 - 1000$ Hz and values of $N_I = 5 - 40$ when monitoring the signal received from a rotating fan. We concluded that the most computationally efficient parameters that would mitigate aliasing were $f_s = 400$ Hz and $N_I = 10$.

As shown in Figure 4, the introduction of a sufficiently large integration time consisting of dense samples significantly improves aliasing. For instance, in Figure 4 (c) we see peaks in the autocorrelation spaced at 1 s, indicating periodicity at a frequency of 1 Hz. We can see, looking at Figure 4 (d), that the inclusion of an integration time

drastically limits aliasing at such low frequencies. Similarly, comparing Figure 4 (e) and Figure 4 (f), we can see the elimination of spikes in the power spectrum on that are separated by 1Hz.

While the integration time reduced the amount of aliasing, we still can see in Figure 4 (d) peaks in the autocorrelation corresponding to frequencies lower than 60 Hz. The same can be said about the Figure 4 (f) where we see peaks in the power spectrum at frequencies other than 60 Hz. This is due to the fact that we are not dealing with a pure sinusoidal signal, and we need a very high sampling frequency to totally eliminate aliasing. However, for the purposes at hand, the residual aliasing is tolerable as far as it does not overlap with frequency component associated with human movements. In other words, as long as the fan generates frequency components that can be used to distinguish its presence from a human, we can rely on post processing to deduce human presence, as discussed in Section V.

IV. SIMULATION ACCURACY

For the proposed ray tracing simulation platform to be useful, it needs to be representative of real-life scenarios. In this section we attempt to reproduce experimental results obtained in a physical cavity [30]. In doing so, we also demonstrate the benefits of generating and sampling multiple masks using DMAs in simulation. The data presented in Figures 6, 11, 12 were all acquired in simulation; we do not present any of the experimental data from [30] in this paper.

To emulate the scenario examined in [30], we defined a 2D geometry which is the cross-section of the 3D cavity used in [30]. This setup, referred to as *Room 2*, is shown in Figure 5. It is important to note that while we attempt to reproduce the experimental results of [30], several factors limit us from obtaining the identical results in our numerical simulation. Firstly, as stated before, our simulations only capture reflections from surfaces and ignore diffraction. Additionally, we are only considering rays within a maximum number of bounces. Further, our simulation is limited in its ability to fully emulate the disorder of a physical cavity. In physical cavities, such as a rooms, disorder is a byproduct of having people, chairs, objects and a constantly evolving geometry. Various material surfaces—and, thus, different microwave reflectivities—introduce another layer of disorder. This disorder generates the diverse modes that the DMA can capitalize on. We attempted to emulate disorder to some extent, as seen in Figure 5, by introducing irregular shapes. However, we did not model each surface as having its own microwave reflectivity. Lastly, by reducing our simulation to 2D, we may lose many reflections or variations that may have contributed to the ability to detect movements.

Since the experiments in [30] were conducted with metallic walls, we assumed the reflectivity coefficient R (see Appendix A), 0.9. With more reflection, rays can bounce more than 3 times before they become statistically insignificant. After redoing the studies discussed in Appendix B, with $R = 0.9$, we decided to increase the reflection cap

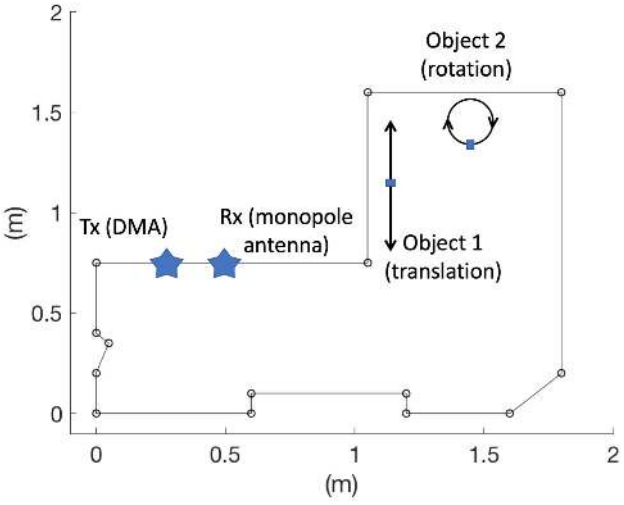

FIGURE 5. A cross-section of *Room 2*: the cavity used in [30]. This is the exact geometry used in simulation. Walls are metallic and rays are capped at 6 reflections. Compare to Figure 1(a) in [30].

to 6. In [30], an approximately 11×11 cm^2 DMA was used as the Tx aperture and a monopole antenna as the Rx antenna. To emulate this configuration, we modeled the DMA as a line of 15 dipoles separated by $\frac{\lambda}{2}$, corresponding to an 11.25 cm long array at 20 GHz. Additionally, [30] tested the configuration where an open-ended waveguide (OEWG) was used as the Tx antenna in lieu of a DMA; this configuration was modeled using a single dipole as the Tx antenna. The Rx antenna was always modeled as a single dipole.

To study the ability to detect motion, [30] used two objects: 1) an aluminum corner on a linear rail which we emulated by a 5 cm square periodically translating over a distance of 55cm with periodicity of 1 s (the blue square on a vertical, two-sided arrow in Figure 5) and 2) an aluminum block on rotation stage which was emulated by a 5 cm square rotating around an axis 5 cm away from its center at 2.3 Hz. We then programmed the periodic movements listed in Table 2:

TABLE 2. Motion schedule used for false negative rate analysis.

0-10s	Translation only
10-20s	Rotation only
20-30s	Both

This simulation resulted in a raw measurement matrix, $S_{i,k}(t)$, as defined in Section II-A, where $i \in \{1, 2, .., 15\}$ is one of the Tx dipoles, $k = 1$ is a single Rx dipole, and $t \in \{0, \frac{1}{f_s}, .., 30\}$ is time, measured in seconds. For simplicity, we chose to sample at $f_s = 40$ Hz. While this low sampling frequency may be inadequate for detecting high frequency content (as discussed earlier), it is high enough to detect motion at frequencies less than 3 Hz. Masks were simulated in the manner discussed in Section II-A to generate $W(t, m)$—similar to notation used in [30]—where m is one of 300 masks with randomly generated phase and binary amplitude. To emulate the conditions in [30], we added complex, white

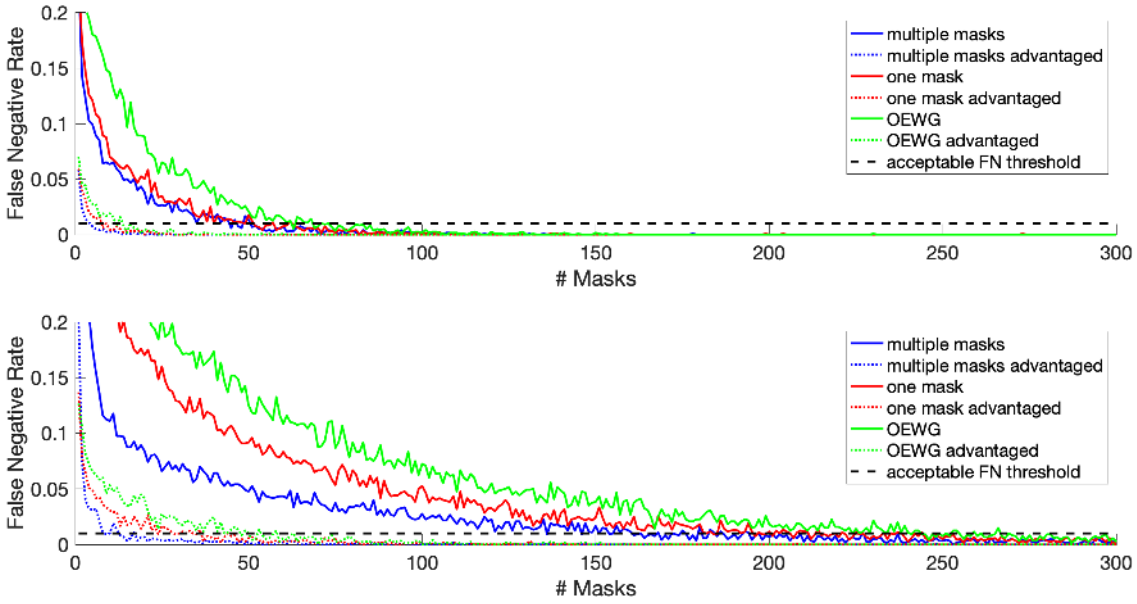

FIGURE 6. Comparing the accuracy of different detection systems in *Room 2* (metal walls, reflection cap = 6) using ray-tracing simulation data. Tx is a 15-dipole array, Rx is a single dipole. The top plot shows false negative rates for different antenna configurations when Rx captures both amplitude and phase information. The bottom plot shows false negative rates for different antenna configurations when Rx only captures amplitude information. Detection accuracy is improved by use of phase information as well as use of multiple masks. Compare to Figure 4(c,d) in [30].

Gaussian noise (WGN) to $W(t, m)$ with a standard deviation equal to that of the measurements in [30].

In Appendix C we have analyzed the return signal and the effect of using different masks in obtaining higher fluctuation of the return signal for small movements in occluded areas. Similar results are also reported in the experiments of [30]. Next, we focus on the ability to detect motion. As in [30], most of our analysis is based on the difference signal, D, which contains the fluctuation of the received signal, as defined:

$$D(t_i) = \text{opt}\Big(|W(t_{i+1}, m) - W(t_i, m)| \Big)_m \tag{6}$$

Similar to (3), we used the difference from subsequent measurements to sift out the dynamic component of the signal while eliminating the background. However, in contrast to (3), we were concerned with variation, and not the direction of variation. Thus, we took the absolute value of this difference. Finally, to lower the dimensionality of the data, we used $\text{opt}()_m$ to denote optimization over all masks. In [30], this optimization equated to averaging over all the masks. However, we explored taking the maximum of all variation from different masks in this discussion as an alternative method to project the data into one dimension.

To further highlight the fact that the ray tracing simulation platform is a reasonable representation of the physics of actual cavities, we computed the false negative rates for the motion schedule of Table 2. To do this, we began by setting a threshold, D_{thresh}, the fluctuation above which is an indication of movement. In [30], D_{thresh} is defined as a function of the standard deviation of measurements taken in a motionless room (thus noise). Similarly, we defined the threshold as:

$$D_{\text{thresh}} = 2.5 \times \text{SD(WGN)}. \tag{7}$$

In the motion schedule considered here, motion is always occurring; as a result, if a received signal fluctuation falls below the threshold in (7), consider that as as a false negative. Low false negative rates are strongly desired in smart sensing schemes; we can see in Figure 6 that using the DMA significantly reduces false negative rates.

We can also augment our detection process by using *a priori* knowledge: when using a system sampling at several hundred Hz (potentially kHz) we can assume that motion occurring at one time sample must still occur at least in the subsequent or prior samples. We searched for points in our normal signals where data fell below D_{thresh} at t_i but was above D_{thresh} at t_{i-1} or t_{i+1} and considered these points true positives. The false negatives rates when using this augmented detection process are also plotted in Figure 6 and labeled as *advantaged*. We clearly see that using some prior knowledge can bring DMA sensor false negative rates to a very low value, acceptable for most applications.

We also investigated the possibility of further simplifying the sensor circuitry by examining the case that the receiver does not detect phase and measures intensity only. Phase detection has the potential to improve false negative rates because it allows the sensor to detect a variation between subsequent measurements which have the same intensity but a different phase. Loss of this capability means that measurements with the same intensity but different phase will fall below our threshold and the system will report no motion.

Data emulating the output of intensity only sensors is also plotted in Figure 6; clearly, intensity only measurements have higher false negative rates.

Moreover, we can make observations about the benefit of using a DMA for motion detection by examining the data presented in Figure 6. We see that employing various masks (versus taking many measurements of a fixed configuration or using a simple omnidirectional antenna) decreases the rate of false negative readings. When the mask configuration is fixed, or when a simple dipole is being used, the only benefit gained from repeatedly taking measurements is the ability to average out noise. By using different masks, we can probe different cavity modes, allowing our system to detect movements in any location with high fidelity. We also know from Figure 12 that different masks pick up on different temporal variations in the room. Thus, multiple masks generate a diverse set of measurements that can benefit from optimization methods. In contrast to the mean used in [30], we used the maximum of variation in these plots as the method of optimization. We did not attempt to explore many different methods and do not make conclusions about what may be the best way to utilize such diverse measurements. Further studies are needed before any such conclusion can be made. What these data *do* demonstrate is that using the DMA to multiplex diverse cavity modes provides a wide distribution of measurements that can be used to detect motion better than the measurements from a fixed antenna configuration.

Most importantly, these results align with the ones presented in [30] demonstrating the utility of our ray tracing simulation platform. As discussed in the beginning of this section, the inability to fully emulate disorder limits our simulation's accuracy. However, the general trends presented in this section fall in line with those presented in [30] and substantiate our assertion that our ray tracing simulations capture salient features of the wave propagation inside a cavity or a room as it pertains to motion detection.

V. TEMPORAL SIGNAL ANALYSIS AND FEATURE EXTRACTION

Detecting motion alone is not sufficient for the proposed device to act as an *occupancy* sensor. It also needs to distinguish the source of motion, i.e. whether it is a human or non human. In previous works, this distinction has been made using Doppler or micro-Doppler shifts due to human movement [14], [49]. Similarly, WiFi-based sensors monitor channel state information [17], [22]. Such classification schemes are only useful when using a finite bandwidth. Even when using high frequency bandwidth, such scenarios are complicated and usually rely on complicated processing of channel state information or expensive learning algorithms.

The single frequency operation of our sensor prevents us from using previous methods based on micro-Doppler shifts. To combat this problem, we note that one of the distinct features of using DMAs as the center hardware of occupancy sensors is the fact that they can vary their masks at a high rate and obtain reliable detection for a large portion of a room, even in occluded areas (as demonstrated in the previous section). This fast acquisition rate also means we can retrieve the temporal signature of the movements inside the room. These signatures can be used to distinguish between different types of motion. In this section, we examine this possibility.

First, we demonstrate that the temporal patterns of the fluctuating signal received by our sensor corresponds to a specific type of motion (rapidly rotating fan, stationary breathing human, a walking human, etc.). Toward this goal, we examined the motion schedule in Table 3 in *Room 1*. In this table, we have also used color coding to further distinguish different types of movement.

TABLE 3. Motion schedule used in classification analysis.

$0-15$s	cyan	Person moves and breathes
$15-30$s	yellow	Fan spins at 57 Hz
$30-40$s	green	Both motions occur

In the first part of this motion schedule, a moving person is modeled by a 40 cm triangle following a random path. Its breathing is modeled by the slight (± 5 mm) sinusoidal variation of the triangle's diameter. In the second part of the motion schedule, we simulated a fan spinning which is modeled by a rotating 40 cm triangle. If one motion is occurring, the other shape remains in the room but does not move or rotate. This assumption allows us to identify the signatures of each motion, contrast them against each other, and evaluate how they superimpose in the third part of this motion schedule.

For this simulation, we set Tx to be a DMA modeled by 8 dipoles and we set Rx to be a single dipole. The mask-optimized signal corresponding to this motion is shown in Figure 7 (a) and is calculated accordingly, where we optimize over 100 possible masks.

$$D_{\mathrm{m,o}}(t) = \max\Big(|D(m,t)| \Big)_m \tag{8}$$

Its corresponding temporal spectrogram, computed using 0.2 Hz frequency resolution and 0.3 second temporal resolution, is shown in Figure 7 (b).

Examining Figures 7 (a) and 7 (b), we can discern some interesting signatures. Aperiodic motion of a person following a random path is characterized by a relatively arbitrary signal signature with drastic variations in signal magnitude due to blocking/unblocking of the sensor. A rotating fan, on the other hand, results in almost periodic variations, with temporal periodicity much higher than most human-induced movements. The superposition of these two motion patterns results in a periodic signal ''corrupted'' with a random signal, indicating the possibility of two motion patterns inside the room.

The spectrogram of the received signal, shown in Figure 7(b), reinforces confidence that motion patterns have characteristic signatures. From $t = 0-15$ s, we do not see any dominant frequency content. From $t = 15-30$s, we see bands at high frequencies with significant power concentration.

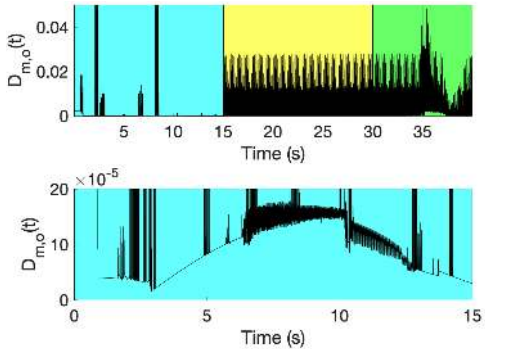

(a) Signal

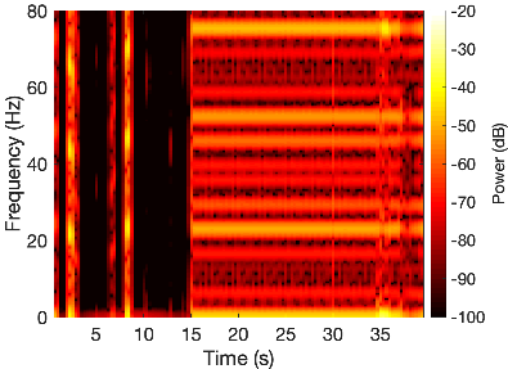

(b) Spectrogram

FIGURE 7. **(a) The difference signal received by our sensor over a 40 second simulation containing the motion schedule summarized in Table II. This simulation was done in *Room 1* with wooden walls and a ray reflection cap of 3. Tx is an 8-dipole array, Rx is a single dipole. The entire simulation is given in the top plot. An expanded portion of the 0-15s interval is given in the bottom plot for clarity. (b) A spectrogram of the 40 second simulation.**

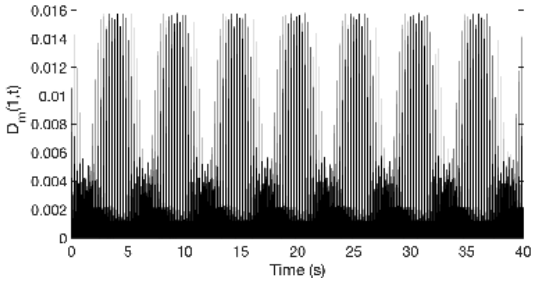

(a) Signal

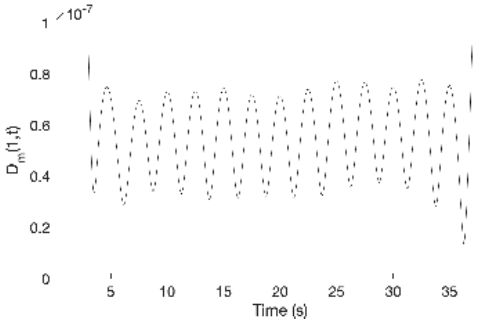

(b) Spectrogram

FIGURE 8. **(a) The temporal difference signal obtained from a simulation where a stationary person breathes at 0.2 Hz while a fan spins at 57 Hz. This simulation was done in *Room 1* with wooden walls and a reflection cap of 3. Tx is an 8-dipole array, Rx is a single dipole. (b) The temporal difference signal above, after application of a Hann window lowpass filter.**

One of these bands occurs at the fan's rotation frequency (approximately $\approx$ 57 Hz); other bands are the result of spectral leakage caused by aliasing of the signal. This is largely an artifact of our simulation's lack of noise and simple geometry. For the last 10 seconds we can see characteristics associated with both motion patterns: the high frequency content from the fan and *random* perturbations caused by the obstructing, moving person.

These plots instill confidence in several factors. Firstly, we can see that our simulation produces the expected results for different motion patterns. An aperiodically moving person produces an aperiodic signal with little to no predictable patterns. High-frequency motion produced by a rotating fan produces periodic signals. Thanks to anti-aliasing sampling, we are able to pick out the frequency of rotation down to 1 Hz. Finally, when both motion patterns superimpose, we can find signatures of both.

In another simulation, we modeled what a detector might see on a warm summer night. In one corner of the room, a person is stationary and breathing at 0.2 Hz. In another corner of the room, a fan rotates at around 57 Hz. Figure 8 (a) shows the temporal difference signal from mask 1, $D_{\mathrm{m}}(1, t)$. In this case, both objects were not translating and, thus, it wasn't necessary to sample and optimize over multiple masks.

The data collected by our sensor is presented in Figure 8. Upon first inspection, it might not seem that a person is present. By applying a Hann window lowpass filter with cutoff at 1 Hz, however, we can easily identify the periodic signature of breathing at 0.2 Hz.

VI. CONCLUSION

In this paper, we outlined a simple and fast ray tracing simulation platform that can be used to explore the potential of dynamic metasurface apertures in detecting and characterizing motion in a room. We demonstrated that its results capture salient features of experimental ones previously reported. Using this simulation tool, we were also able to reaffirm the notion that DMAs' many spatially distinct radiation patterns significantly improve the capability to detect motion, even when there is no line of sight between transmitters and receivers.

Having a reliable simulation platform is useful for future development of this sensor. Firstly, we can design and test motion patterns that may be impossible to generate physically; we can repeat this testing with exact precision in a way not possible in experiment. Additionally, being able to define and test cavity geometries quickly allows us to explore the potential of this technology without having to reconstruct or find new physical cavities—some of which may be physically impractical to build or impossible to find.

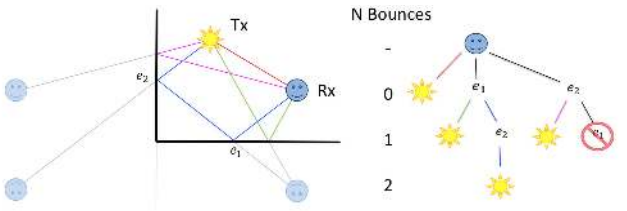

FIGURE 9. (left) Visualization of ray tracing algorithm and application of image theory. (right) Corresponding recursion tree, showing all ray paths from Rx radiator to Tx radiator. The path Rx-e_2-e_1-Tx is not possible using only specular reflection and is pruned.

Finally, we demonstrated that the motion signatures generated by this simulation platform can be analyzed to generate predictions about sources of those motions. In this paper, we demonstrated that simple Fourier transformations and filters provided insight into motion signatures that were not explicitly obvious initially. This can be taken a step further. In future work we hope to demonstrate that learning algorithms can be trained with these data patterns. With enough training, algorithms as simple as support vector machines can not only detect motion, but characterize it.

APPENDIX A
RAY TRACING MODEL

The ray tracing algorithm computes all eligible paths between the Tx antennas indexed by $i \in \{1, 2, \ldots, N_{TX}\}$, and the Rx antennas indexed by $k \in \{1, 2, \ldots, N_{RX}\}$. Our simulation only accounts for specular reflection using image theory [50], and neglects diffraction and refraction. More specifically, the algorithm begins from the k_{th} Rx radiator and checks whether any of the Tx radiators are visible or not; if that is the case, a ray between the Tx antenna and the Rx antenna is"drawn." Next, the algorithm generates a list of all edges that are visible to the k_{th} Rx antenna and uses image theory to compute its images about all those edges. Looking through the edge that was used to produce the images, the algorithm then determines whether any of the Tx antennas are visible to any of the images of the k_{th} Rx antenna. This process repeats until a reflection limit is reached; the limit is necessary to prevent an infinite runtime. Essentially, ray tracing is a recursive algorithm where the base case is where a reflection point is visible to the receiver. Each iteration is brought on by reflection about an edge. This approach, historically used in many ray tracing implementations [37], [38], is visually illustrated in Figure 9.

For each ray, we track the amplitude decay and phase accumulation as it travels from Tx to Rx. The signal due to ray, r from the ith Tx dipole to the kth Rx dipole is given by $S_{i,k}(r)$:

$$S_{i,k}(r) = \frac{R^{B_{i,k}(r)}}{D_{i,k}(r)} e^{-j\beta D_{i,k}(r)} \tag{9}$$

where R is the reflection coefficient for walls and objects, $B_{i,k}(r)$ is the number of times the ray reflects off of surfaces, $D_{i,k}(r)$ is the distance of the ray, and β is the free space wavenumber. All dipoles output the same power, determined by the number of active dipoles in a mask (see Section IV.A).

The operation frequency considered in this paper is 20 GHz, which is the same as the one used in [30]. This frequency of operation allows for an antenna with high sensitivity and a small foot print. Single frequency operation significantly simplifies the transceiver design and lowers cost compared to broadband transceivers. Moreover, as discussed in the introduction, by operating at a single frequency and using omnidirectional patterns, the sensor can easily avoid interference at higher frequencies. If interference is a concern, the proposed sensor can easily be modified to operate within an ISM band, such as at 24 GHz.

Assuming 20 GHz operation, the attenuation constant, R, is selected based on empirical results available in [51]. We use the reflection coefficient for wood, due to its ubiquity in residential and commercial construction, and because it has high attenuation relative to other common building materials over K-band [51]. We also assume the reflection attenuation does not change significantly with the incident angle as has been shown empirically in [51]. Assuming the worst-case scenario in our material parameters implies that results from these simulations should only improve if a set of materials more representative of actual buildings are used in simulation.

APPENDIX B
REFLECTION LIMIT

An important factor influencing the accuracy of the described algorithm is the limit on the number of ray bounces, N_b. As this number increases, the accuracy of the model improves at the cost of longer simulation times. Since rays incur significant attenuation with reflections and longer paths, there is diminishing return in accuracy to increasing the number of bounces. To this end, we searched for an optimal limit on N_b to navigate this trade-off by running a repeatable simulation of an object moving along an arbitrary path throughout the room. Because we are solely concerned with the accuracy of the system under different recursion caps, we only used a single Tx and single Rx for this simulation. We ran this simulation with different caps on the maximum reflections, as shown in Figure 10(a).

To highlight the diminishing return, we have calculated the average relative percent error, as defined below. We use $S(t, B_{\max}) = \sum_r S_{1,1}(r)$ to denote the receiver signal at a time t with a maximum number of bounces, $B_{\max}$.

$$\mathrm{RE}(B_{\max}) = \left\langle \frac{|S(t, B_{\max}) - S(t, 5)|}{S(t, 5)} \times 100 \right\rangle_t \tag{10}$$

In this case, we have only used a single dipole for Tx and Rx. $\langle\rangle_t$ denotes averaging over all time. S(t,5), the signal for a system with a maximum number of bounces equal to 5, was used here as the *ground truth*.

As shown in Figure 10 (b), there is minimal signal contribution for rays beyond 3 bounces, which exhibit relative errors

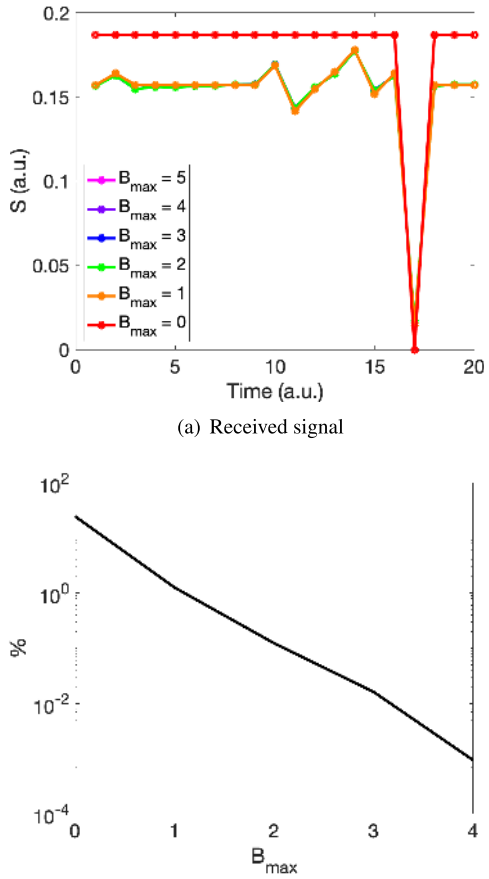

(a) Received signal

(b) Relative error

FIGURE 10. **(a) The received signal with different B_{max} for a 20 frame simulation of a subject following an arbitrary path through *Room 1*. Walls are wooden, Tx/Rx are single dipoles. (b) The average percent error over all frames for various B_{max}, relative to the case where $B_{max} = 5$.**

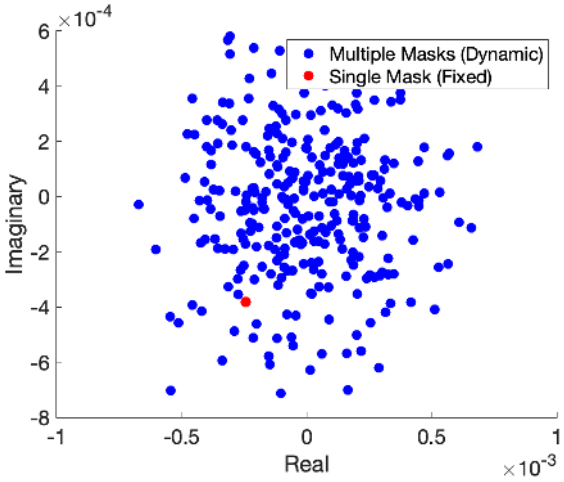

FIGURE 11. ***W*(t_i, *m*) for 300 different masks (blue) and for 300 measurements with a fixed mask configuration (red) using ray-tracing simulation data. The spread of the blue points demonstrates the variety offered by multiple masks. The spread of the red points is only due to noise in the signal. Data obtained in *Room 2* with metallic walls and a ray reflection cap of 6. Tx is a 15-dipole array, Rx is a single dipole. Compare to Figure 3(a) in [30].**

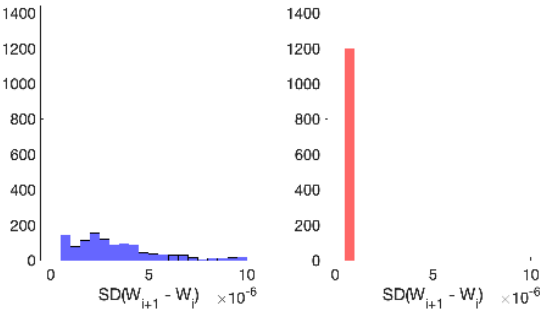

FIGURE 12. **Histograms of the quantity *Z*, for signals obtained in multiple mask (left) and fixed mask (right) configurations for ray-tracing simulation data. Data obtained in *Room 2* with metallic walls and a ray reflection cap of 6. Tx is a 15-dipole array, Rx is a single dipole. Compare to Figure 3(d,e) in [30].**

below 0.01%. Thus, given the potentially exponential runtime complexity dependence on the reflection limit, we only consider up to 3 reflections throughout this paper as a compromise between convergence and runtime, unless otherwise stated.

APPENDIX C
UTILITY OF DMA IN DETECTING MOTION

In Figure 11 we plot a single row of W (masks at a single time instance) from both varied and fixed mask configurations. In the varied mask configuration, each column in W was generated using a distinct and randomly generated mask. In the fixed mask configuration, the same mask was used to generate data for each column; any variance in this case is the result of the addition of WGN. As we see, the varied mask data has a larger spread in the complex domain than the fixed mask data, demonstrating that sampling various masks achieves a level of variation higher than that of the noise.

As in [30], we have demonstrated that signal variation with multiple masks at a single point in time exceeds the magnitude of variation caused by noise, implying that variation is due to the sampling of various masks. To further highlight this point, we defined the quantity Z as:

$$Z(t_i) = \mathrm{SD}\Big(|W(t_{i+1}, m) - W(t_i, m)|\Big)_m, \tag{11}$$

which is the standard deviation over all masks for the difference between subsequent measurements. As discussed in [30], Z attempts to demonstrate empirically that different masks serve to sample different mode variations in the room. The histogram of values of Z are plotted in Fig. 12. In a noiseless environment, we expect to have $Z = 0$ for the fixed mask case because a single mask can only probe variation in one mode; thus, the difference between subsequent measurements will have no spread. Even with noise, as in Figure 12, Z forms a tight distribution about zero for the fixed mask case. In contrast, when using multiple masks, we observe different levels of variation, indicating each mask is probing different set of cavity modes.

Figures 11 and 12 demonstrate that our simulation exhibits trends similar to those depicted in [30]. These results also reaffirm our understanding that using different masks provides signal variation above the standard deviation of noise, especially between subsequent measurements.

ACKNOWLEDGMENT

The views and opinions of authors expressed herein do not necessarily state or reflect those of the United States Government or any agency thereof.

REFERENCES

[1] L. Atzori, A. Iera, and G. Morabito, "The Internet of Things: A survey," *Comput. Netw.*, vol. 54, no. 15, pp. 2787–2805, Oct. 2010.
[2] G. P. Hancke, B. de Carvalho e Silva, and G. P. Hancke, Jr., "The role of advanced sensing in smart cities," *Sensors*, vol. 13, no. 1, pp. 393–425, 2012.
[3] P. López-Iturri, E. Aguirre, L. Azpilicueta, J. J. Astrain, J. Villandangos, and F. Falcone, "Challenges in wireless system integration as enablers for indoor context aware environments," *Sensors*, vol. 17, no. 7, p. 1616, 2017.
[4] Y. Agarwal, B. Balaji, R. Gupta, J. Lyles, M. Wei, and T. Weng, "Occupancy-driven energy management for smart building automation," in *Proc. 2nd ACM Workshop Embedded Sens. Syst. Energy-Efficiency Building*, 2010, pp. 1–6.
[5] T. A. Nguyen and M. Aiello, "Energy intelligent buildings based on user activity: A survey," *Energy Buildings*, vol. 56, pp. 244–257, Jan. 2013.
[6] J. Lu, T. Sookoor, V. Srinivasan, G. Gao, B. Holben, J. Stankovic, E. Field, and K. Whitehouse, "The smart thermostat: Using occupancy sensors to save energy in homes," in *Proc. 8th ACM Conf. Embedded Netw. Sensor Syst.*, 2010, pp. 211–224.
[7] F. Adib, H. Mao, Z. Kabelac, D. Katabi, and R. C. Miller, "Smart homes that monitor breathing and heart rate," in *Proc. 33rd Annu. ACM Conf. Hum. Factors Comput. Syst.*, 2015, pp. 837–846.
[8] F. Lin, Y. Zhuang, C. Song, A. Wang, Y. Li, C. Gu, C. Li, and W. Xu, "SleepSense: A noncontact and cost-effective sleep monitoring system," *IEEE Trans. Biomed. Circuits Syst.*, vol. 11, no. 1, pp. 189–202, Feb. 2017.
[9] A. Arcelus, M. H. Jones, R. Goubran, and F. Knoefel, "Integration of smart home technologies in a health monitoring system for the elderly," in *Proc. 21st Int. Conf. Adv. Inf. Netw. Appl. Workshops*, May 2007, pp. 820–825.
[10] H. Wang, D. Zhang, Y. Wang, J. Ma, Y. Wang, and S. Li, "RT-Fall: A real-time and contactless fall detection system with commodity WiFi devices," *IEEE Trans. Mobile Comput.*, vol. 16, no. 2, pp. 511–526, Feb. 2017.
[11] L. Z. Rubenstein, "Falls in older people: Epidemiology, risk factors and strategies for prevention," *Age Ageing*, vol. 35, no. 2, pp. ii37–ii41, 2006.
[12] H. Liu, Y. Wang, K. Wang, and H. Lin, "Turning a pyroelectric infrared motion sensor into a high-accuracy presence detector by using a narrow semi-transparent chopper," *Appl. Phys. Lett.*, vol. 111, no. 24, 2017, Art. no. 243901.
[13] T. Teixeira, G. Dublon, and A. Savvides, "A survey of human-sensing: Methods for detecting presence, count, location, track, and identity," *ACM Comput. Surv.* vol. 5, no. 1, pp. 59–69, 2010.
[14] E. Yavari, C. Song, V. Lubecke, and O. Boric-Lubecke, "Is there anybody in there?: Intelligent radar occupancy sensors," *IEEE Microw. Mag.*, vol. 15, no. 2, pp. 57–64, Mar. 2014.
[15] S. Palipana, B. Pietropaoli, and D. Pesch, "Recent advances in RF-based passive device-free localisation for indoor applications," *Ad Hoc Netw.*, vol. 64, pp. 80–98, Sep. 2017.
[16] M. Amin, *Radar for Indoor Monitoring: Detection, Classification, and Assessment*. Boca Raton, FL, USA: CRC Press, 2017.
[17] S. Depatla, A. Muralidharan, and Y. Mostofi, "Occupancy estimation using only WiFi power measurements," *IEEE J. Sel. Areas Commun.*, vol. 33, no. 7, pp. 1381–1393, Jul. 2015.
[18] Y. Wang, J. Liu, Y. Chen, M. Gruteser, J. Yang, and H. Liu, "E-eyes: Device-free location-oriented activity identification using fine-grained WiFi signatures," in *Proc. 20th Annu. Int. Conf. Mobile Comput. Netw.*, 2014, pp. 617–628.
[19] K. Muthukrishnan, M. Lijding, N. Meratnia, and P. Havinga, "Sensing motion using spectral and spatial analysis of WLAN RSSI," in *Proc. Eur. Conf. Smart Sens. Context*. Springer, 2007, pp. 62–76.
[20] J. A. Nanzer, "A review of microwave wireless techniques for human presence detection and classification," *IEEE Trans. Microw. Theory Techn.*, vol. 65, no. 5, pp. 1780–1794, May 2017.
[21] Q. Xu, Y. Chen, B. Wang, and K. J. R. Liu, "Radio biometrics: Human recognition through a wall," *IEEE Trans. Inf. Forensics Security*, vol. 12, no. 5, pp. 1141–1155, May 2017.
[22] C. Wu, Z. Yang, Z. Zhou, X. Liu, Y. Liu, and J. Cao, "Non-invasive detection of moving and stationary human with WiFi," *IEEE J. Sel. Areas Commun.*, vol. 33, no. 11, pp. 2329–2342, Nov. 2015.
[23] B. Wang, Q. Xu, C. Chen, F. Zhang, and K. R. Liu, "The promise of radio analytics: A future paradigm of wireless positioning, tracking, and sensing," *IEEE Signal Process. Mag.*, vol. 35, no. 3, pp. 59–80, May 2018.
[24] G. Maret, "Diffusing-wave spectroscopy," *Current Opinion Colloid Interface Sci.*, vol. 2, no. 3, pp. 251–257, 1997.
[25] J. de Rosny, P. Roux, M. Fink, and J. H. Page, "Field fluctuation spectroscopy in a reverberant cavity with moving scatterers," *Phys. Rev. Lett.*, vol. 90, no. 9, 2003, Art. no. 094302.
[26] S. G. Conti, J. de Rosny, P. Roux, and D. A. Demer, "Characterization of scatterer motion in a reverberant medium," *J. Acoust. Soc. Amer.*, vol. 119, no. 2, p. 769, 2006.
[27] G. Lerosey and J. de Rosny, "Scattering cross section measurement in reverberation chamber," *IEEE Trans. Electromagn. Compat.*, vol. 49, no. 2, pp. 280–284, May 2007.
[28] S. G. Conti, P. Roux, D. A. Demer, and J. de Rosny, "Measurement of the scattering and absorption cross sections of the human body," *Appl. Phys. Lett.*, vol. 84, no. 5, p. 819, 2004.
[29] J. De Rosny and P. Roux, "Multiple scattering in a reflecting cavity: Application to fish counting in a tank," *J. Acoust. Soc. Amer.*, vol. 109, no. 6, p. 2587, 2001.
[30] P. del Hougne, M. F. Imani, T. Sleasman, J. N. Gollub, M. Fink, G. Lerosey, and D. R. Smith, "Dynamic metasurface aperture as smart around-the-corner motion detector," *Sci. Rep.*, vol. 8, p. 6536, Apr. 2018.
[31] T. Sleasman, M. F. Imani, W. Xu, J. Hunt, T. Driscoll, M. S. Reynolds, and D. R. Smith, "Waveguide-fed tunable metamaterial element for dynamic apertures," *IEEE Antennas Wireless Propag. Lett.*, vol. 15, pp. 606–609, 2016.
[32] T. Sleasman, M. F. Imani, J. N. Gollub, and D. R. Smith, "Dynamic metamaterial aperture for microwave imaging," *Appl. Phys. Lett.*, vol. 107, no. 20, 2015, Art. no. 204104.
[33] T. Sleasman, M. F. Imani, J. N. Gollub, and D. R. Smith, "Microwave imaging using a disordered cavity with a dynamically tunable impedance surface," *Phys. Rev. Appl.*, vol. 6, Nov. 2016, Art. no. 054019.
[34] T. Sleasman, M. Boyarsk, M. F. Imani, J. N. Gollub, and D. R. Smith, "Design considerations for a dynamic metamaterial aperture for computational imaging at microwave frequencies," *J. Opt. Soc. Amer. B, Opt. Phys.*, vol. 33, no. 6, pp. 1098–1111, Jun. 2016.
[35] L. Pulido-Mancera, T. Fromenteze, T. Sleasman, M. Boyarsky, M. F. Imani, M. Reynolds, and D. Smith, "Application of range migration algorithms to imaging with a dynamic metasurface antenna," *J. Opt. Soc. Amer. B, Opt. Phys.*, vol. 33, no. 10, pp. 2082–2092, Oct. 2016.
[36] A. V. Diebold, L. Pulido-Mancera, T. Sleasman, M. Boyarsky, M. F. Imani, and D. R. Smith, "Generalized range migration algorithm for synthetic aperture radar image reconstruction of metasurface antenna measurements," *J. Opt. Soc. Amer. B, Opt. Phys.*, vol. 34, no. 12, pp. 2610–2623, Dec. 2017.
[37] J. W. McKown and R. L. Hamilton, Jr., "Ray tracing as a design tool for radio networks," *IEEE Netw.*, vol. 5, no. 6, pp. 27–30, Nov. 1991.
[38] M. C. Lawton and J. P. McGeehan, "The application of GTD and ray launching techniques to channel modelling for cordless radio systems," in *Proc. 42nd Veh. Technol. Soc. Conf.*, May 1992, pp. 125–130.
[39] S. Y. Seidel and T. S. Rappaport, "A ray tracing technique to predict path loss and delay spread inside buildings," in *Proc. GLOBECOM*, Dec. 1992, pp. 649–653.
[40] D. I. Laurenson, S. McLaughlin, and A. U. H. Sheikh, "The application of ray tracing and the geometrical theory of diffraction to indoor channel modelling," in *Proc. IEEE Global Telecommun. Conf.*, Nov./Dec. 1993, pp. 1242–1246.
[41] J. B. Andersen, T. S. Rappaport, and S. Yoshida, "Propagation measurements and models for wireless communications channels," *IEEE Commun. Mag.*, vol. 33, no. 1, pp. 42–49, Jan. 1995.
[42] C.-F. Yang, B.-C. Wu, and C.-J. Ko, "A ray-tracing method for modeling indoor wave propagation and penetration," *IEEE Trans. Antennas Propag.*, vol. 46, no. 6, pp. 907–919, Jun. 1998.

[43] Z. Ji, B.-H. Li, H.-X. Wang, H.-Y. Chen, and T. K. Sarkar, "Efficient ray-tracing methods for propagation prediction for indoor wireless communications," *IEEE Antennas Propag. Mag.*, vol. 43, no. 2, pp. 41–49, Apr. 2001.
[44] L. Azpilicueta, F. Falcone, and R. Janaswamy, "A hybrid ray launching-diffusion equation approach for propagation prediction in complex indoor environments," *IEEE Antennas Wireless Propag. Lett.*, vol. 16, pp. 214–217, 2016.
[45] A. Ishimaru, *Wave Propagation and Scattering in Random Media*, vol. 12. Hoboken, NJ, USA: Wiley, 1999.
[46] V. Degli-Esposti, D. Guiducci, and A. de'Marsi, P. Azzi, and F. Fuschini, "An advanced field prediction model including diffuse scattering," *IEEE Trans. Antennas Propag.*, vol. 52, no. 7, pp. 1717–1728, Jul. 2004.
[47] C. Clinic. (2019). *Vital Signs*. [Online]. Available: https://my.clevelandclinic.org/health/articles/10881-vital-signs
[48] A. D. Yaghjian, "An overview of near-field antenna measurements," *IEEE Trans. Antennas Propag.*, vol. 34, no. 1, pp. 30–45, Jan. 1986.
[49] W. Butler, P. Poitevin, and J. Bjomholt, "Benefits of wide area intrusion detection systems using FMCW radar," in *Proc. 41st Annu. IEEE Int. Carnahan Conf. Secur. Technol.*, Oct. 2007, pp. 176–182.
[50] C. A. Balanis, *Modern antenna handbook*. Hoboken, NJ, USA: Wiley, 2011.
[51] B.-G. Choi, W.-H. Jeong, and K.-S. Kim, "Characteristics analysis of reflection and transmission according to building materials in the millimeter wave band," *Power (dBm)*, vol. 13, nos. 50–62, pp. 48–64, 2015.

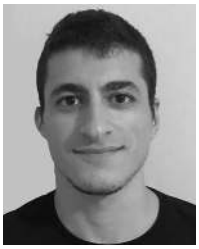

OREN S. MIZRAHI (S'19) received the B.S.E. degree in biomedical engineering and the B.S.E. degree in electrical and computer engineering from Duke University, Durham, NC, USA, in 2019. He is currently pursuing the Ph.D. degree in electrical engineering with the California Institute of Technology, Pasadena, CA, USA.

He joined the Center for Metamaterials and Integrated Plasmonics, Duke University, in 2018, as an undergraduate Pratt Fellow. From 2018 to 2019, he was involved in the development of metasurface-based sensing systems.

MOHAMMADREZA F. IMANI (M'08) received the B.S.E. degree in electrical engineering from the Sharif University of Technology, Tehran, Iran, in 2007, and the M.S.E. and Ph.D. degrees in electrical engineering from the University of Michigan, Ann Arbor, MI, USA, in 2010 and 2013, respectively.

From 2014 to 2018, he has served as a Postdoctoral Associate with the Department of Electrical and Computer Engineering, Duke University, Durham, NC, USA, where he is currently a Research Scientist. He has authored or coauthored over 70 journals and conference papers. He holds one granted and five pending patent applications. His research interests include analytical and applied electromagnetics, metamaterials and metasurfaces, microwave imaging and sensing, wireless power transfer, antenna analysis and synthesis, and MIMO communication systems.

K. PARKER TROFATTER received the B.Eng. degree in engineering physics and the B.Eng. degree in computer science from The University of Tennessee, Knoxville, TN, USA, in 2011. He is currently pursuing the Ph.D. degree in electrical and computer engineering from Duke University, Durham, NC, USA.

He joined the Center for Metamaterials and Integrated Plasmonics, Duke University, in 2013, as a Lab Technician, supporting the research and development of novel microwave compressive sensing imaging funded by the DHS.

JONAH N. GOLLUB received the B.A. degree in physics from Reed College, in 2000, and the Ph.D. degree in physics from the University of California at San Diego, San Diego, in 2009. His thesis work covered a variety of metamaterial focused topics, including the hybridization of metamaterials with magnetic materials and the demonstration of magnetic surface plasmon polaritons on metamaterials. From 2010 to 2013, he was a Lead Modeling and Simulation Scientist with a startup company, developing surface metamaterials, with applications for imaging and biological detection under DARPA, MDA, Army, and NSF funded efforts. He joined Duke University as a Research Scientist, in 2013, with a focus on the development of a real-time millimeter wave imaging system utilizing frequency diverse metasurface antennas and computational imaging techniques.

DAVID R. SMITH (M'03–SM'18) received the B.S. and Ph.D. degrees in physics from the University of California at San Diego, San Diego, CA, USA, in 1988 and 1994, respectively. He is currently a James B. Duke Professor of electrical and computer engineering with Duke University and the Director of the Center for Metamaterials and Integrated Plasmonics. His research interests include the theory, simulation, and characterization of unique electromagnetic structures, including photonic crystals and metamaterials, and applications of such materials. He has provided key experimental demonstrations in the metamaterials field, including the first demonstration of a negative index metamaterial, in 2000 and the first demonstration of a metamaterial invisibility cloak, in 2006. He was elected as a Fellow of the National Academy of Inventors, in 2016. He was a co-recipient of the Descartes Scientific Research Prize awarded by the European Union, in 2005 and the James C. McGroddy Prize for New Materials, awarded by the American Physical Society, in 2013. Since 2009, he has been listed as a Highly Cited Researcher by Clarivate Analytics in the field of physics.